

ARTICLE

Open Access

# Detection of cracked teeth using a mechanoluminescence phosphor with a stretchable photodetector array

Ha Jun Kim<sup>1</sup>, Sangyoon Ji<sup>2</sup>, Ju Yeon Han<sup>1</sup>, Han Bin Cho<sup>1</sup>, Young-Geun Park<sup>2</sup>, Dongwhi Choi<sup>3</sup>, Hoonsung Cho<sup>4</sup>, Jang-Ung Park<sup>1,2</sup> and Won Bin Im<sup>1</sup>

## Abstract

Cracked tooth syndrome (CTS) is an incomplete fracture of a human tooth that commonly arises from chewing hard foods. Although it is a very common syndrome, CTS is often difficult to diagnose owing to the common small size of tooth cracks. Conventional techniques for the detection of cracks, such as transillumination and radiographic methods, are inaccurate and have poor imaging resolution. In this study, we devise a novel method for the *in vivo* detection of tooth microcracks by exploiting the mechanoluminescence (ML) phenomenon.  $\text{ZrO}_2:\text{Ti}^{4+}$  (ZRT) phosphor particles are pasted onto suspected regions of tooth cracks and emit cyan-colored light as a result of masticatory forces. Then, a stretchable and self-healable photodetector (PD) array laminated on top of the phosphor particles converts the emitted photons into a photocurrent, which facilitates the two-dimensional mapping of the tooth cracks. Because of the high photosensitivity of the PD, intense ML and small size of ZRT phosphor particles, it is possible to image submicron- to micron-sized cracks with high resolution. Furthermore, the uniqueness of this technique over the conventional techniques stems from the application of a simple optical phenomenon, i.e., ML, for obtaining precise information regarding the locations, depth, and length of tooth cracks.

## Introduction

The recent change in the eating habits of humans in modern society has caused a series of syndromes, including cracked tooth syndrome (CTS). CTS is on the rise due to the prolongation of life expectancy in humans and consequently prolonged use of teeth. CTS refers to an incomplete tooth fracture whereby the enamel and dentin of teeth are instantly or gradually broken or separated by an external force<sup>1,2</sup>. This syndrome causes a sharp pain sensation in teeth while drinking cold beverages or biting hard foods, which desists upon the release of masticatory

pressure<sup>3,4</sup>. Habits that might lead to CTS include aging dentition, chewing ice or foods with small and sharp objects (e.g., seeds), or dental injuries<sup>5</sup>. Diagnosing this syndrome is often complicated because the cracks are usually too small to be observed by the naked eye.

Tooth staining with a dye<sup>6</sup>, transillumination<sup>7</sup>, and radiographic techniques such as intraoral X-ray imaging, cone-beam computed tomography, and microcomputed tomography (micro-CT) has been employed to diagnose dental problems<sup>8</sup>. Gentian violet or methylene blue stains have been utilized to mark fracture lines. The drawback of this method is that it requires a minimum of 2–5 days to be effective and often fails to differentiate craze lines (scratches that do not require any treatment) from tooth cracks<sup>9</sup>. The transillumination technique can be used to detect all types of tooth cracks, from craze lines to root fractures, but without differentiation<sup>10</sup>. The resolution of radiographic techniques is too low to detect cracks

Correspondence: Jang-Ung Park ([jang-ung@yonsei.ac.kr](mailto:jang-ung@yonsei.ac.kr)) or Won Bin Im ([imwonbin@hanyang.ac.kr](mailto:imwonbin@hanyang.ac.kr))

<sup>1</sup>Division of Materials Science and Engineering, Hanyang University, Seoul 04763, Republic of Korea

<sup>2</sup>Department of Materials Science and Engineering, Nano Science Technology Institute, Yonsei University, Seoul 03722, Republic of Korea

Full list of author information is available at the end of the article

These authors contributed equally: Ha Jun Kim, Sangyoon Ji, Ju Yeon Han

© The Author(s) 2022



**Open Access** This article is licensed under a Creative Commons Attribution 4.0 International License, which permits use, sharing, adaptation, distribution and reproduction in any medium or format, as long as you give appropriate credit to the original author(s) and the source, provide a link to the Creative Commons license, and indicate if changes were made. The images or other third party material in this article are included in the article's Creative Commons license, unless indicated otherwise in a credit line to the material. If material is not included in the article's Creative Commons license and your intended use is not permitted by statutory regulation or exceeds the permitted use, you will need to obtain permission directly from the copyright holder. To view a copy of this license, visit <http://creativecommons.org/licenses/by/4.0/>.

smaller than  $100\ \mu\text{m}$ <sup>11</sup>. In addition, radiation exposure involved in these methods is hazardous to the patient's health. Micro-CT has gained much attention in dental research owing to its high-resolution images obtained by X-ray attenuation<sup>12</sup>. Nevertheless, this technique is not suitable for the *in vivo* detection of tooth cracks. Recently, optical coherence tomography (OCT) has shown potential for detecting very small tooth cracks with high resolution, with no risk of radiation exposure<sup>13</sup>. However, OCT suffers from image contrast problems, especially in areas with low contrast between the background and signal<sup>14</sup>. Moreover, most of these techniques require sophisticated equipment. Owing to these drawbacks, it has been difficult to detect tooth cracking at early stages, which can eventually lead to irreversible and complete fracture of the tooth. Furthermore, secondary infections, whereby bacteria infiltrate into the internal nerve tissue, may occur as the cracking progresses. Hence, the development of a simple and less time-consuming method is necessary to efficiently detect submicron- and micron-sized tooth cracks. In this study, we introduce a unique way of detecting microcracks by exploiting the mechanoluminescence (ML) property of an inorganic phosphor. ML is a light emission process whereby a solid material undergoes elastic deformation and luminesces upon the application of an external stress<sup>15</sup>. The recombination of charge carriers under mechanical stimuli leads to light emission from these phosphors. To date, ML phosphors have been mainly limited to stress field sensing and electric and magnetic field sensing<sup>16,17</sup>. Nevertheless, in this report, we apply the ML phenomenon for the first time for the detection of CTS.

Herein, we demonstrate the early diagnosis of CTS by imaging the microcracks on a tooth in the closed mouth condition using an ML phosphor and a stretchable and self-healable photodetector (PD) array that can conformably cover a single tooth. The ML phosphor was first pasted onto the suspected tooth crack area and was then covered with the PD array. Upon the application of a masticatory force, the phosphor material emits photons (light), which are collected by the PD array and are converted into a photocurrent, providing information on the depth, width, length, and position of the microcracks. Because it is possible to synthesize phosphor particles of various sizes, we can detect submicron-sized tooth cracks with a highly photosensitive PD array. It must be noted that light emission occurs only if stress is applied to the phosphor particles. Thus, unlike traditional methods, such as transillumination, our technique can clearly distinguish cracks from the craze lines because, when the phosphor particles are attached to the craze lines, they do not experience human masticatory stress and hence do not emit light. Moreover, this method does not require sophisticated equipment and hence will be useful in the

early diagnosis of CTS. To the best of our knowledge, this is the first report on the use of ML for the detection of the position and size of tooth cracks.

## Experimental

### Synthesis of the materials

The ZRT powder samples were prepared with a solid-state method. The starting materials consisting of stoichiometric amounts of  $\text{ZrO}_2$  (Kojundo, 99.9%) and  $\text{TiO}_2$  (Aldrich, 99.9%) were ground in an agate mortar, placed in alumina crucibles, and fired at  $1300\text{--}1500\ ^\circ\text{C}$  for 4 h in a tubular furnace using a 5%  $\text{H}_2/95\% \text{N}_2$  gas mixture. After the heat treatment, the samples were naturally cooled to room temperature and ground with an agate mortar into a fine powder for further analysis and application.

### Determination of crystal structure

Structural measurements of the powder samples were conducted via the high-resolution powder diffraction (HRPD) beamline (9B) at Pohang Accelerator Laboratory was employed for the experiments. During the measurements,  $\theta/2\theta$  with a fixed time of 1 s and a step size of  $0.01^\circ$  for  $2\theta = 0\text{--}130^\circ$  and a beamline with a wavelength of  $1.52250\ \text{\AA}$  were used. Structural information of the as-synthesized samples was derived by refinement using the General Structural Analysis System<sup>18</sup>. The background coefficient, zero-point, and asymmetry parameter for the peak shape, scale factor, and unit-cell parameters were refined until convergence was achieved. The VESTA program was used to draw the crystal structure<sup>19</sup>. The particle size and morphology were analyzed via high-resolution-transmission electron microscopy (HR-TEM). HR-TEM images and elemental mapping were obtained using an FEL Tecani F20 from the Korea Basic Science Institute, Gwangju. Surface analysis measurements were performed via X-ray photoelectron spectroscopy (XPS) using a VG Multilab 2000.

### Optical measurements

Thermoluminescence (TL) measurements were recorded using stimulated luminescence with a TL/OSL-DA 20 luminescence reader (Risø DTU, Denmark) equipped with a  $90\text{Sr}/90\text{Y}$   $\beta$ -ray source at a dose rate of  $3.6\ \text{Gy}/\text{min}$ . The temperature ranged from 0 to  $450\ ^\circ\text{C}$ . The photoluminescence (PL) spectra of the samples were measured using a Hitachi F-4500 fluorescence spectrophotometer equipped with a 150 W xenon lamp over the wavelength range of  $200\text{--}650\ \text{nm}$ . The ML properties were measured using a homemade instrument (stress gauge and photomultiplier tube [PMT]). To evaluate the ML properties of ZRT, powders were mixed with polydimethylsiloxane (PDMS) to form cylindrical discs with a diameter of 2.5 cm and a thickness of 1 cm. PDMS is used as a matrix

to transmit the stress of the ZRT powder grains. In this way, the ML samples were prepared in phosphor-to-PDMS ratios of 1:10, 1:9, and 2:8. After a 20 s optical excitation, a compressive strain was applied to the samples while measuring the emitted light. A PMT equipped with an optical fiber was used to record the intensity of the ML emitted by the samples, and the corresponding images were recorded by a digital camera (EOS 80D, Canon).

#### Numerical simulation of ZRT in a tooth crack

A numerical simulation was conducted by using the commercial software COMSOL Multiphysics. The tooth was represented as a cylinder, and the corresponding radius ( $r$ ) and height ( $h$ ) of the tooth were set to 1 and 2 cm, respectively. The location of the crack was fixed in the center of the tooth. Young's moduli of enamel (the main constituent of teeth) and  $ZrO_2$  were set to 80 and 200 GPa, respectively. Poisson's ratios of enamel and  $ZrO_2$  were set to 0.3 and 0.22, respectively. The average human masticatory force (approximately 500 N) was applied on the top surface of the tooth in three directions (horizontal, 45° tilted, and vertical).

#### Fabrication of stretchable PDs

A sacrificial layer of Cu (thickness: 700 nm) was deposited on a bare Si wafer by a thermal evaporator, followed by spin coating of a 1- $\mu$ m-thick epoxy adhesive layer (SU-8, Microchem Corp.). The top Si layer of silicon on insulator wafer (300 nm of Si on 400 nm of buried oxide, Soitec) was photolithographically patterned with reactive ion etching (RIE) to a channel dimension of  $50 \times 150 \mu\text{m}$ . The buried oxide layer was etched using an HF solution; then, the Si channels were picked up using a PDMS stamp. After transferring the Si channels onto the epoxy surface, Cr/Au (2/150 nm), which served as the source and drain, was evaporated and patterned. To obtain stretchable and self-healable interconnections (thickness: 2  $\mu\text{m}$ ), an Ag nanoparticle ink (NPK, Korea; average diameter:  $40 \pm 5 \text{ nm}$ ) containing 70 wt% LM microcapsules as a self-healing agent was coated and dried at 130 °C for 10 min for patterning using photolithography. Then, a 30-nm-thick  $Al_2O_3$  layer was deposited using an atomic layer deposition system before patterning. Subsequently, gate electrodes were formed using the Ag-LM composite. For the fabrication of the stress-tunable rigid-soft hybrid substrates, mechanically reinforced islands (SU-8, 25  $\mu\text{m}$ ) of a negative photoresist were patterned with dimensions of  $250 \times 250 \mu\text{m}$ . Then, an elastomeric layer of PDMS (thickness: 45  $\mu\text{m}$ ) was spin-coated and cured to embed the reinforced islands successively. After removing the Cu sacrificial layer by wet etching, the resulting sample was flipped over. Then, the

epoxy adhesion layer was etched using RIE, and a 45- $\mu$ m-thick PDMS layer was coated to encapsulate the devices.

#### Characterization of stretchable PDs

The electrical performances, such as transfer, output characteristics, and real-time sensing of the PD array, were measured using a probe station (Keithley 4200-SCS). To measure the optical responses of the PDs, a halogen lamp (300–700 nm wavelength) was used as a visible light source with an optical filter. The stretchability test of the PD array was conducted using a step motor controller (ECOPIA) with a frequency of 0.5 Hz.

#### Cytotoxicity test of ZRT phosphor powder

L-929 fibroblast cells were cultured in the Roswell Park Memorial Institute (RPMI) 1640 medium supplemented with 10% FBS, nonessential amino acids, sodium pyruvate, vitamin A, and glutamine at 37 °C in a humidified incubator under an atmosphere of 5%  $CO_2$ . Cells in the exponential growth phase were harvested by a 2-min treatment with a 0.25% trypsin/0.02% EDTA solution and maintained by periodic dilutions with a fresh medium. The effects of ZRT on in vitro cell viability were evaluated using the MTT [3-(4,5-dimethylthiazol-2-yl)-2,5-diphenyltetrazolium bromide] assay. L-929 cells were plated in 100  $\mu\text{L}$  RPMI 1640 at a density of 5000 cells in a 96-well plate. After an overnight incubation culture period, cells were exposed for three days with different concentrations of phosphor particles at 37 °C under standard cell culture conditions. RPMI 1640-10% FBS was used as vehicle control. 3-(4,5-Dimethylthiazol-2-yl)-2,5-diphenyltetrazolium bromide (2 mg/mL in PBS) was added to the cultures at 0.02 mL per well during the final 2 h of incubation. The medium was then carefully removed, and dark blue formazan was dissolved in 100  $\mu\text{L}$  per well of DMSO. The absorbance of each well was measured with a Varioskan Lux microplate reader (Thermo Scientific, Waltham, MA) at 570 nm. The percentages of cell viability were calculated according to  $(\text{Abs } 570 \text{ nm of treated group} / \text{Abs } 570 \text{ nm of the control group}) \times 100$ .

#### ML imaging of a microcracked tooth using the stretchable PD array

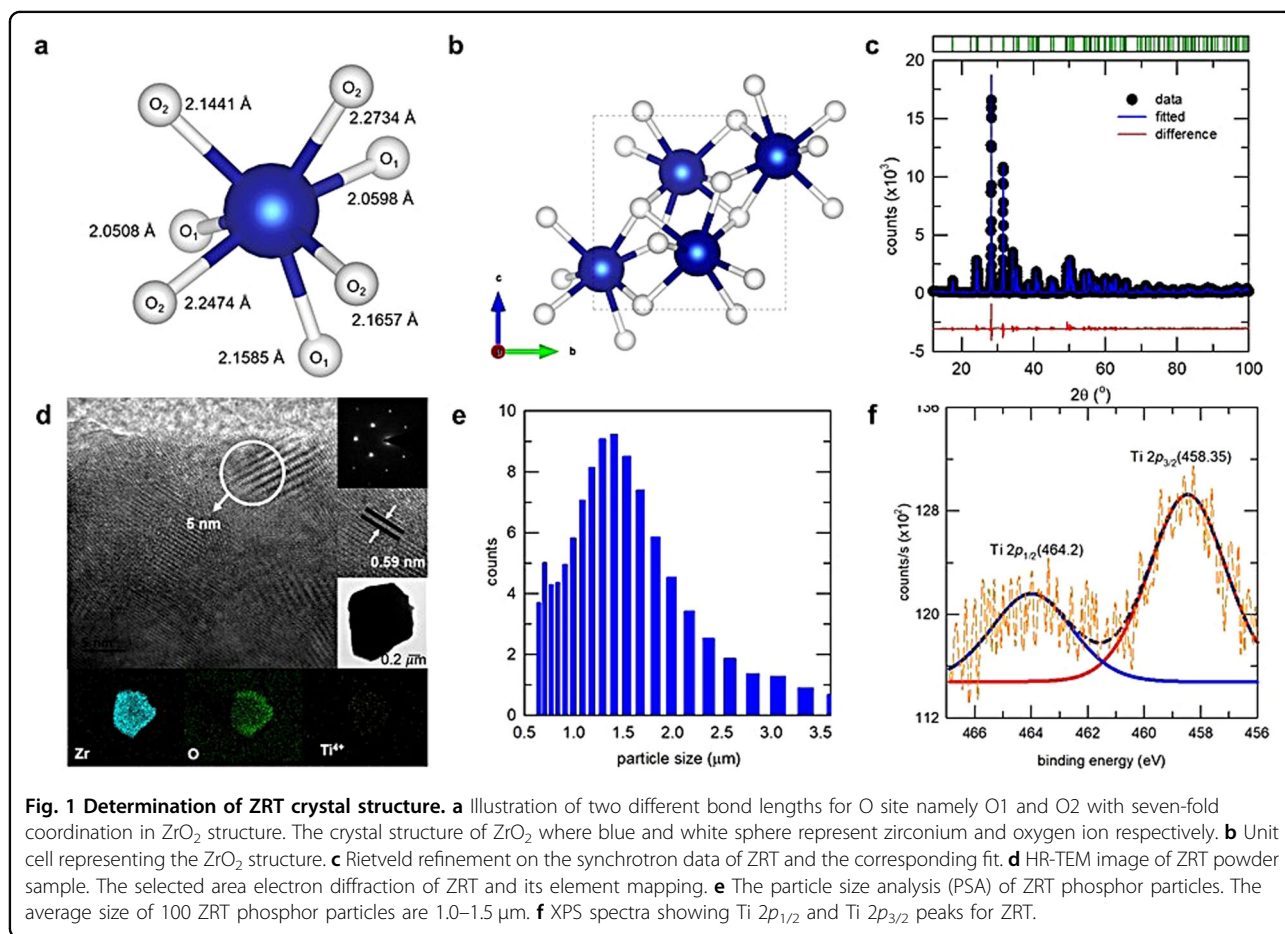
The denture for real-time CTS detection was purchased from Health Edco. To mimic human masticatory movement, a well-defined compressive force was applied using a motorized z-axis stage (Mark-10 ESM303). The compressive force was measured using a force gauge (Mark-10 M7-100). For the real-time image mapping of the ML emission, a sourcemeter (Keithley 2400), system switch (Keithley 3706), relay card (Keithley 3723), and peripheral devices were used to interconnect the PD array with custom-made processing modules.

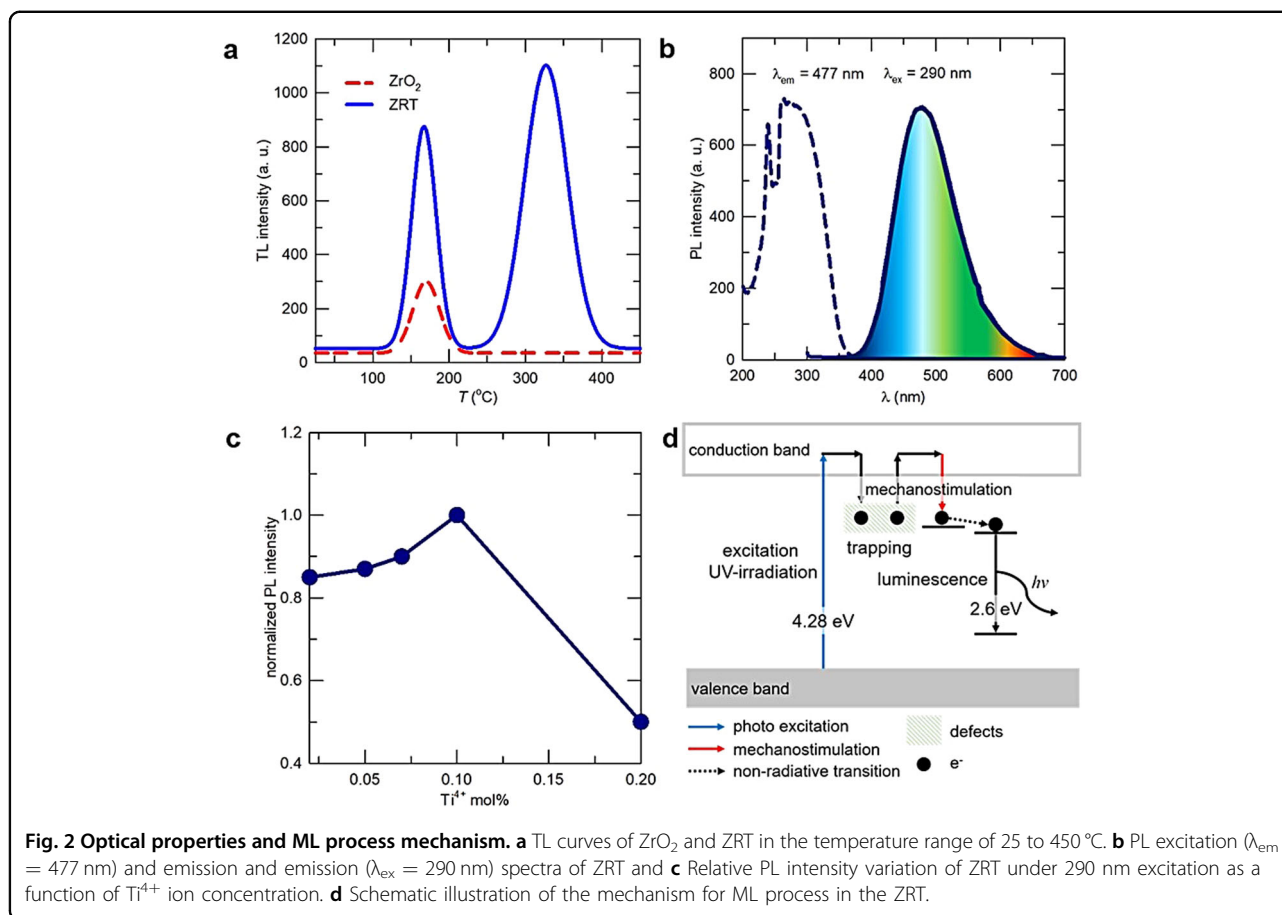
## Results and discussion

### ZrO<sub>2</sub>:Ti<sup>4+</sup> (ZRT) as the ML phosphor

For in vivo dental applications, materials should withstand high mechanical pressures and should not compromise the health of patients. There are a few well-known classes of phosphors that exhibit interesting ML properties<sup>20,21</sup>. These include phosphors based on alkali halides and silicates doped with lanthanide ions<sup>22</sup>; however, the presence of lanthanide ions makes these ML phosphors bioincompatible, owing to their toxicity. Doped II–VI semiconductors, such as CdS and ZnS, also emit photons upon exposure to external pressure. However, their low mechanical strength and stability make them unsuitable for applications involving high mechanical stresses. ZRT also exhibits interesting ML properties, recovering its ML intensity even upon repetitive application of stress with the aid of UV irradiation<sup>23</sup>. Furthermore, because of its lower chemical reactivity and high mechanical strength, on par with other biomaterials such as alumina, and high hardness (8–8.5 on the Mohs scale), ZrO<sub>2</sub> has been used for ex vivo and in vitro dental restorations, such as crowns, bridges, and implants, and in total hip replacement applications<sup>24,25</sup>. Therefore, ZRT

and its ML properties can be utilized for ex vivo bio applications. Figure 1a shows the unit cell of the ZrO<sub>2</sub> structure. Figure 1b displays a schematic of Zr-O polyhedra. Zr exists in sevenfold coordination, with Zr-O distances ranging from 2.05 to 2.26 Å. O1 is coordinated to three Zr atoms in a planar configuration, and O2 is four-coordinated in a distorted tetrahedral configuration. The two different Zr-O1 and Zr-O2 bond distances are shown in Fig. 1a. The outcomes of Rietveld refinement performed on the synchrotron HRPD pattern of ZRT are shown in Fig. 1c. ZrO<sub>2</sub> was crystallized in the monoclinic *P2<sub>1</sub>/c* space group (Supplementary Tables S1 and S2 and Supplementary Fig. S1), which is in agreement with the literature reports<sup>26,27</sup>. The structural parameters obtained from the refinement of the ZRT monoclinic structure are  $a = 5.146659(24)$  Å,  $b = 5.211275(25)$  Å, and  $c = 5.313711(23)$  Å, as displayed in Supplementary Table S1. The values of the refinement parameters, given in the legend of the table, indicate that the sample is in a single phase without impurities. HR-TEM images and the elemental mapping of the ZRT sample are shown in Fig. 1d. The particle size analysis performed on the HR-TEM images shows that the average ZRT phosphor particle size is



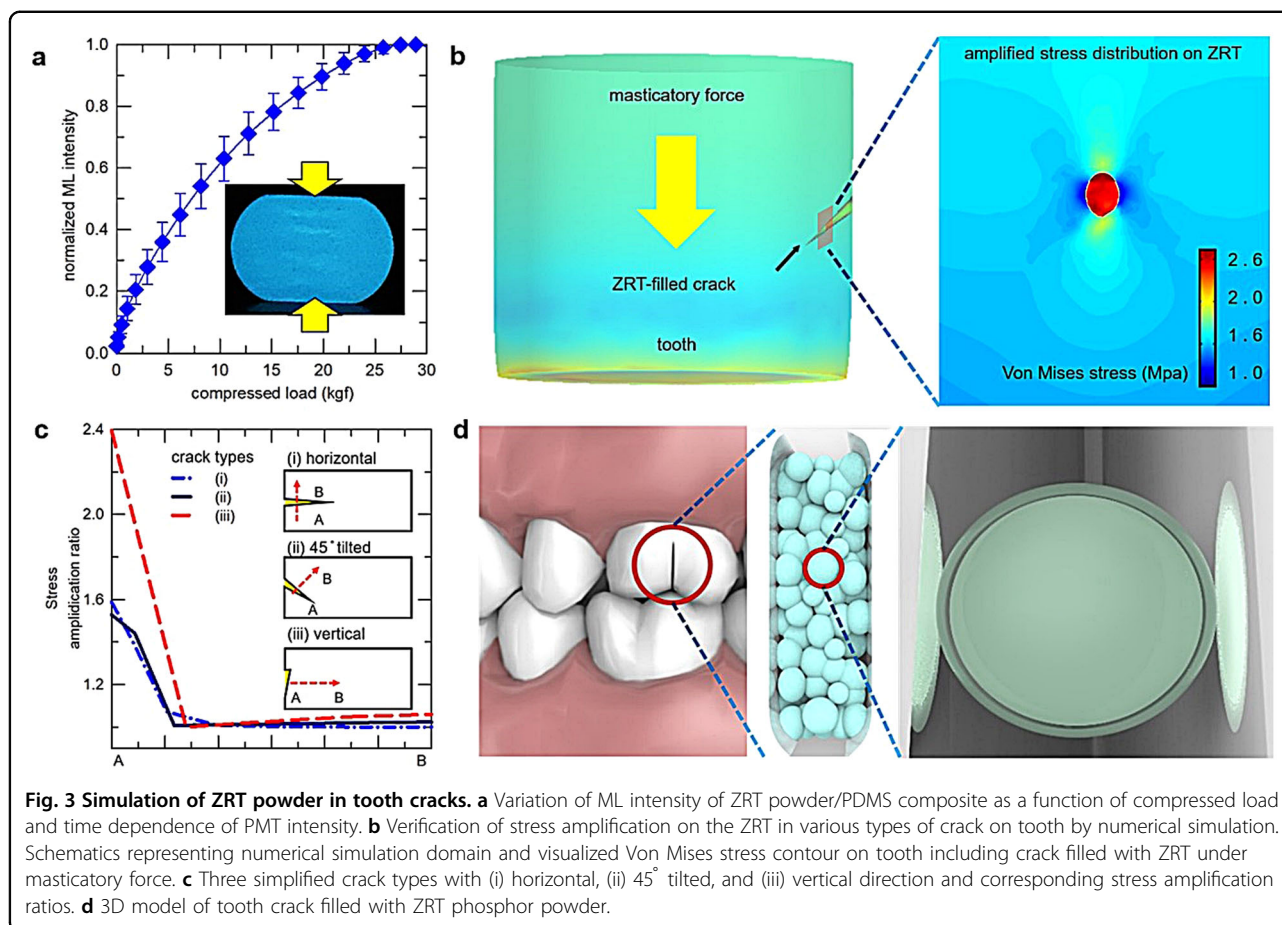


1–3  $\mu\text{m}$ ; the size distribution is presented in Fig. 1e. The elemental mapping results further confirm the presence of small amounts of Ti in the sample, in addition to Zr and O. Furthermore, XPS was employed to determine the oxidation state of Ti, as shown in Fig. 1f. A typical XPS survey spectrum of the ZRT sample was collected at a binding energy range of 0–1150 eV. The Ti 2*p* core-level spectrum occurs at a binding energy range of 450–470 eV, as shown in Fig. 1f. The spectrum displays the spin-orbit splitting characteristics of Ti 2*p* levels and indicates that Ti exists in the +4 oxidation state<sup>28</sup>. The peak present in the 457.5–458.5 eV region can be attributed to Ti 2*p*<sub>3/2</sub><sup>29,30</sup>. The XPS intensity of Ti<sup>4+</sup> ions is weak owing to their very low doping concentration.

#### Light emission from the ML phosphor

Oxygen and zirconium vacancies might be created in pure ZrO<sub>2</sub> during synthesis. To study the defect levels in the ZRT phosphor, which affect the luminescence process when mechanical stress is applied<sup>31</sup>, TL analysis was performed, which probes the trap depth and density in the samples by increasing the temperature<sup>32,33</sup>. Figure 2a shows the TL spectra of the pure ZrO<sub>2</sub> and ZRT samples. ZRT exhibits two prominent defect peaks in its TL

spectrum in the temperature ranges of ~150–200 °C and ~240–400 °C, whereas pure ZrO<sub>2</sub> displays only one defect peak in the ~150–200 °C temperature range. The TL measurements show that trapping centers were created in both samples when they were fired in a 5% H<sub>2</sub>/95% N<sub>2</sub> reduction atmosphere. However, Ti<sup>4+</sup> ion incorporation modified the trap depth/density of pure ZrO<sub>2</sub><sup>34</sup>, which might be responsible for its intense ML and is indicated by the additional peak in its TL spectrum after doping, as shown in Fig. 2a. To obtain further insight into the ML characteristics of ZRT, its photoluminescence excitation (PLE) and PL spectra were measured, as shown in Fig. 2b. The ZRT exhibits a broad emission band at approximately 477 nm (cyan color), assisted by Ti<sup>4+</sup> ions, and the corresponding PLE spectrum shows a broad absorption band in the 200–360 nm region. It is worth noting that the optimum Ti<sup>4+</sup> concentration for obtaining the maximum PL efficiency of the ZRT phosphor particles was found to be 0.1 mol% at room temperature, as shown in Fig. 2c. The study of the TL glow curves and PL spectrum, as well as the XPS results, helps in framing a plausible mechanism for the ML of ZRT, as shown in Fig. 2d. The photo-excitation above the band gap of the ZrO<sub>2</sub> host ( $E_g \approx 4.28$  eV) leads to the transfer of electrons from the valence



band (VB) to the conduction band (CB), which are subsequently captured by the defect levels present in the system<sup>35</sup>. Upon application of mechanical stress, these electrons are detrapped and captured by  $Ti^{4+}$  defect levels through the CB, which lies closely beneath the CB. Then, the captured electrons recombine with the holes present at the energy level above the VB<sup>36</sup> and generate a bright cyan color emission at  $\sim 477$  nm. The absence of ML in the undoped (pure)  $ZrO_2$  might support the  $Ti^{4+}$ -assisted ML hypothesis.

A setup to deform materials was employed to induce the ML phenomenon in the ZRT, and additional devices were employed to collect emitted light. Figure 3a shows the PMT intensity of the ML composite disc under a constant compressive stress rate applied by a compressive system operating at 300 N for 30 s<sup>37</sup>. The composite disc was prepared by adding ZRT phosphor particles to PDMS, which exhibits a cyan-colored ML upon application of stress<sup>38</sup>. The luminescence behavior of the stress-activated ZRT sample was investigated. The luminescence intensity increased as the pressure applied to the sample increased, as shown in Fig. 3a. A schematic three-dimensional model of a tooth crack is shown in Fig. 3d.

The micron-sized ZRT phosphor particles were applied inside the portion of the microsized tooth cracks. These particles emit light through the masticatory force (the maximum masticatory force is 500 N).

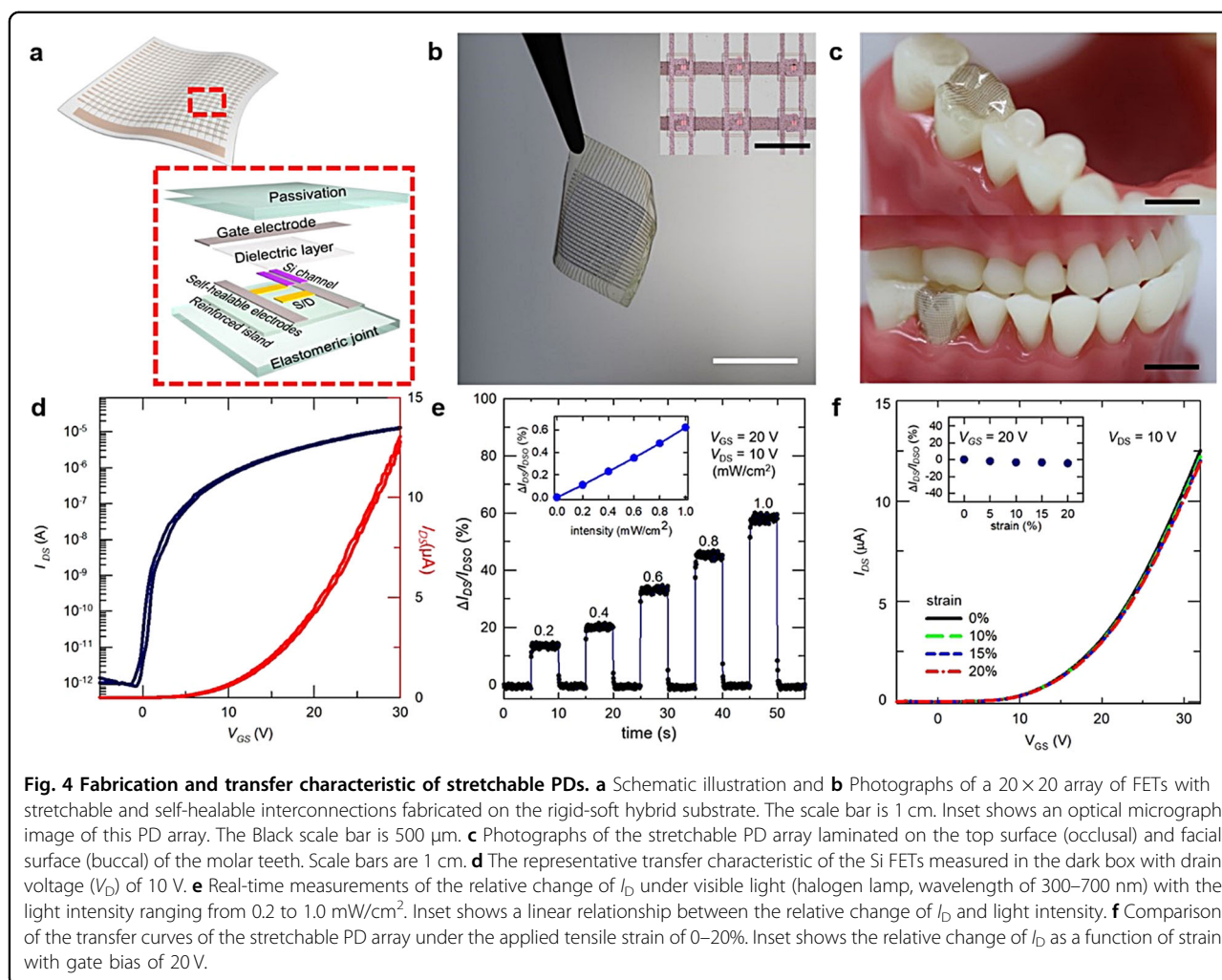
A tooth with a ZRT-filled crack under human masticatory pressure is simplified in the numerical simulation, as shown in Fig. 3b. The tooth is represented by a cylinder, and a masticatory force of 500 N is applied in the vertical direction. In this simulation, only the von Mises stress, which is often used in the scalar form of the effective stress under complex loading conditions, was considered, as shown in Fig. 3b. Owing to differences in Young's modulus and Poisson's ratio between enamel, the main constituent of tooth, and the ZRT present in the tooth crack, an amplified von Mises stress was distributed on the ZRT. To generalize the simulation, three types of cracks were considered: horizontal, 45°-tilted, and vertical; the corresponding stress distributions were calculated numerically, as shown in Fig. 3c. For quantitative analysis, we define the concept of the stress amplification ratio as the ratio of the stress with a crack to that without a crack, which is newly defined and calculated by following the specified line (A to B in Fig. 3c). Figure 3c indicates that

although the amplification ratio depends on the direction of the crack, the presence of the ZRT-filled crack induces amplified stress in all crack types. For a more quantitative investigation of the stress amplification due to the presence of the ZRT-filled crack, further analyses under various masticatory conditions are needed.

#### Stretchable PDs for measuring ML by masticatory force

After pasting the ZRT phosphor particles onto a tooth, a stretchable and self-healable PD array, which can conformably cover its outer surface, was applied to perform high-resolution imaging of the microcracked tooth in a closed mouth condition by monitoring the ML light produced as a result of masticatory forces. Although highly stretchable PDs can be fabricated using free-standing serpentine geometries of metallic interconnections, the large deformation caused by masticatory motion can lead to damage or cracks in these freestanding metals<sup>39,40</sup>. Moreover, the use of semiconducting nanowires or organic semiconductors for stretchable PD arrays

can degrade the uniformity in their electrical properties due to the difficulty in positioning individual nanowires or to organic swelling and dissolution by the oral environment, respectively<sup>41,42</sup>. In this study, instead of free-standing geometries, we fabricated an active-matrix array of PDs using ultrathin single-crystalline Si nanomembranes (thickness: 300 nm) with in-plane stretchable structures. Here, field-effect transistors (FETs) acted as PDs using the generation of photocurrents from their semiconducting channels by absorbing the ML emission induced by masticatory forces, and discrete FETs were protected against these masticatory forces by placing FETs on mechanically reinforced islands of a substrate. These rigid components were linked with elastomeric joints, and stretchable and self-healable electrodes for interconnecting FETs as an active matrix were placed on these soft elastomer areas. This active-matrix form using FETs is advantageous for allowing high spatial resolution and contrast as well as a fast response by minimizing signal crosstalk<sup>43,44</sup>. Figure 4a, b shows the schematic and



photograph, respectively, of a  $20 \times 20$  FET array with stretchable and self-healable interconnections (as an active matrix) fabricated on the rigid-soft hybrid substrate. The detailed fabrication steps are described in Supplementary Fig. S2 and the Methods section. The stretchability of the resulting device is advantageous for its conformal lamination onto the surface of molar teeth (occlusal and buccal sides), as shown in Fig. 4c. Furthermore, the reversible healing ability of the electrodes for interconnecting individual FETs can be advantageous for improving the reliability of this integrated PD array by preventing the permanent disconnection of electrodes when strains beyond the mechanical withstanding limit are applied. Our self-healable electrodes consist of silver (Ag) and a liquid metal (LM, 75.5% gallium, 24.5% indium alloy by weight) and include no polymer for high electrical conductivity ( $\sim 2 \text{ S}/\mu\text{m}$ ). LM microcapsules are uniformly dispersed inside the Ag matrix, forming an Ag-LM composite. This composite film can be patterned for electrode geometries using photolithography and lift-off processes. The self-healing mechanism is schematically described in Supplementary Fig. S3a. The stretchable and self-healing process of this Ag-LM composite includes the following three steps. First, stretching fractures the brittle Ag matrix and rips the thin oxide skin of the LM. Then, the LM can physically flow out and connect adjacent Ag fragments to recover the electrical conductivity of the electrodes. Second, the LM is stretched further by applying an external tensile strain and becomes physically disconnected when the strain exceeds 70%. Third, the disconnected surface of the LM can be wetted and reconnected by releasing the strain, recovering the conductivity of the composite. Supplementary Fig. S3b shows plots of the resistance change of this composite at each step. The LM component enables the instantaneous and natural self-healing of these electrodes (within a few milliseconds) under ambient conditions, as well as high stretchability. Moreover, the inclusion of silver in this liquid metal improves the mechanical strength of this composite, thereby overcoming the limitation of the pristine liquid metal that has low mechanical strength. Supplementary Fig. S4 shows the repetitive cyclic fracturing and self-healing test of the Ag-LM composite electrodes under masticatory movement with a compressive force of 700 N, which exceeds that of humans. The degradation of the electrode resistance due to self-healing is negligible.

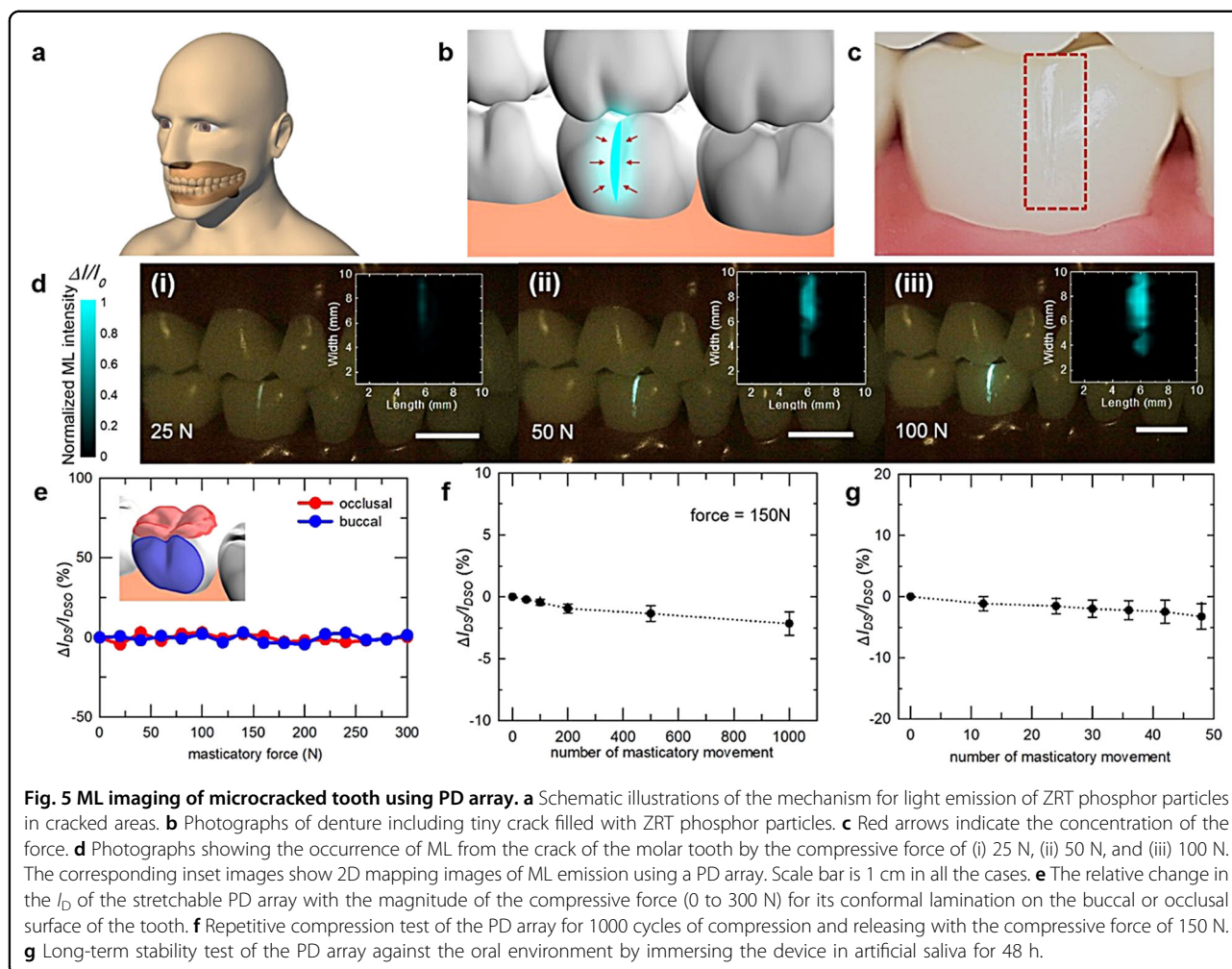
The electrical properties of these stretchable FETs were measured in a dark box. Figure 4d and Supplementary Fig. S5 show the transfer and output characteristics of the stretchable FETs, respectively, with average mobility of  $547 \pm 53 \text{ cm}^2/\text{V}\cdot\text{s}$  in the saturation regime (n-channel). The statistical distribution of the relative change in the field-effect mobility of these 400 FETs in total is provided

in Supplementary Fig. S6, and these data fit Gaussian profiles. Their average on/off ratio and threshold voltage are  $3.4 \times 10^6$  and 13 V, respectively. When the light is irradiated onto the stretchable FETs, the channel areas absorb the light and generate additional photocarriers with increasing drain current (ID) of FETs, which can detect the light emission from the ML composites as PDs. Figure 4e exhibits the photoresponse characteristics of these FETs under visible light (halogen lamp, wavelength of 300–700 nm). Light intensities ranging from 0.2 to  $1.0 \text{ mW}/\text{cm}^2$  can be clearly distinguished by the step-like features; Supplementary Fig. S7 shows their relatively fast response ( $\sim 10 \text{ ms}$ ) and recovery time ( $\sim 15 \text{ ms}$ ). Here, the ID increases linearly with light intensity in the range of 0.2– $1.0 \text{ mW}/\text{cm}^2$ , as shown in the inset of Fig. 4e. It is a value that can be reasonably measured even if the intensity of light decreases as the amount of luminescent material applied to the artificial tooth decreases. In addition, the stretchable FETs exhibit outstanding repeatability with negligible hysteresis during the 100 repetition cycles of light on/off (light intensity:  $0.6 \text{ mW}/\text{cm}^2$ ), as shown in Supplementary Fig. S8. Furthermore, the stability of these FETs against mechanical deformations was tested by stretching the FET array with tensile strains of up to 20%. The Si FETs showed negligible change in their transfer characteristics under the released or stretched conditions, as shown in Fig. 4f. Compared to the resistance of individual FETs in the ‘on state’ ( $\sim 2.1 \times 10^6 \Omega$ ), the resistance of the stretchable interconnections ( $\sim 25 \Omega$ ) is sufficiently small under this deformation, which prevents the degradation of the channel current and circuit delay in the active-matrix array.

#### ML imaging of a microcracked tooth using a stretchable PD array

A cytotoxicity test demonstrated that ZRT is not harmful to the human body, as shown in Supplementary Figs. S9 and S10, in accordance with the literature reports<sup>25,45</sup>. Figure 5 shows high-resolution imaging of a microcracked tooth taken with the active-matrix PD array with a stretchable and self-healable form for the diagnosis of CTS. Figure 5a shows a schematic of the light emission mechanism in ZRT phosphor particles in the cracked areas. Here, cracks were intentionally produced on the surface of the denture (Plaque Hunter Demonstration Model, Health Edco), and ZRT phosphor particles were pasted to fill the cracked areas, as shown in Fig. 5b. Initially, these phosphor particles were exposed to UV radiation ( $\lambda_{\text{ex}} = 254 \text{ nm}$ ) for 20 s. Although the ZRT phosphor particles emitted cyan-colored light during this UV irradiation, as depicted in Fig. 5c, the emission was instantly stopped by turning off the lamp. Nevertheless, the irradiated energy is stored by the ZRT phosphor particles; consequently, they emit intense light upon the





application of masticatory forces (Supplementary Fig. S11). It must be noted that the phosphor particles were irradiated with UV light only before pasting onto the tooth, which prevents the human body from direct exposure to harmful UV radiation. Supplementary Fig. S12 shows the experimental setup consisting of a motorized z-axis stage and a force gauge for applying and measuring the compressive force to the denture, respectively. As shown in Fig. 5d and Supplementary Fig. S13, the light intensity emitted from the pasted phosphor particles increased when the compressive force increased from 25 to 100 N. Photographs of the ML emission from the tooth crack were taken for an open-mouth model using a digital camera (EOS 80D, Canon) without using the PDs. However, this digital camera imaging method cannot be applied in a closed mouth condition. Therefore, the PD array was necessary for imaging in the closed mouth condition. The insets of Fig. 5d show 2D mapping images of the ML emission from the tooth crack using this PD array after the application of 25, 50, and 100 N compressive forces. This PD array monitored the ML of

the tooth crack clearly. The ML images (insets of Fig. 5d) are similar to those taken using the digital camera (Fig. 5d). This shows that the PD array is a reliable technique for ML imaging of tooth cracks. The PD array also detected an increase in the ML intensity with the compressive load. The stretchable nature of the PD array enabled conformal covering of the tooth surface with negligible gaps, which is advantageous to minimize image distortions due to refraction or scattering of light.

The self-healing ability of the PD array is advantageous for its reliable operations during masticatory pressure. For example, Fig. 5e plots the relative change in its ID (photocurrent) with the magnitude of the compressive force for its conformal lamination on the buccal or occlusal surface of the tooth. When the sample was attached to the buccal surface, the change in photocurrent due to the masticatory force was negligible. Although the device was directly compressed between the upper and lower teeth while laminating the occlusal region, the relative change in photocurrent was also negligible, similar to the buccal case, because the elastomeric parts of the substrate acted

as a buffer layer and the rigidly reinforced parts protected individual devices with no cracks. A compressive force of 150 N was repeatedly applied to the PD array laminated on the occlusal surface. As shown in Fig. 5f, this device operated stably with negligible change in photocurrent (less than 5%) after 1000 cycles of compression and release. Furthermore, the stability of this PD array against the oral environment was studied by storing it in artificial saliva (Fusayama–Meyer artificial saliva, Pickering Laboratories, Inc.) for 48 h. Figure 5g shows its reliable operations without significant degradation in the photocurrent even after 48 h. The inorganic device structures as well as the rigid-soft hybrid passivation enabled its good stability.

## Conclusions

In this work, we demonstrated the detection of smaller tooth cracks in a unique way by exploiting the ML phenomenon, which helps in the early diagnosis of CTS. TL and PL measurements suggest that  $Ti^{4+}$  dopants are responsible for the ML observed in the ZRT by introducing additional defect levels in the  $ZrO_2$ . A stretchable and self-healable PD array is developed with an active-matrix form that exhibits high operational stability against masticatory stresses and strong resistance to photo-degradation and can be conformably and reversibly laminated onto the surface of ZRT-pasted teeth. The PD array aids the ex vivo imaging of tooth cracks by converting the ML from the ZRT phosphor particles into a photocurrent. Owing to the high photosensitivity of the PD and the intense ML and small size of the ZRT phosphor particles, it is possible to image submicron- to micron-sized cracks with high resolution. This is further supported by the successful mapping of tooth microcracks with a low masticatory force of 25 N. This technique allows the ex vivo high-resolution imaging of small tooth cracks and does not require sophisticated equipment. Thus, our technique facilitates the successful detection of submicron-sized tooth cracks in their early stage of formation, which in turn prevents irreversible damage due to tooth cracking. It is noteworthy that our work broadens the applications of the ML phenomenon by applying it in biomedical sciences.

## Acknowledgements

This work was supported by the National Research Foundation of Korea (NRF) grant funded by the Ministry of Education (NRF-2018H1A2A1062877) and the Korean government (MSIT) (NRF-2021M3H4A1A02049634, 2020M3H4A3081792), the Bio & Medical Technology Development Program (NRF-2018M3A9F1021649), Nano Material Technology Development Program (NRF-2021M3D1A204991411). This work was supported by the BK21 FOUR (Fostering Outstanding Universities for Research) program through the National Research Foundation (NRF) funded by the Ministry of Education of Korea. This research was also supported by the Technology Innovation Program (KEIT-20010737) and the Korea Initiative for Fostering University of Research and Innovation (KIURI) Program (2020M3H1A1077207), Center for

Super Critical Material Industrial Technology (20013621) funded by the Ministry of Trade, Industry & Energy (MOTIE, Korea).

## Author details

<sup>1</sup>Division of Materials Science and Engineering, Hanyang University, Seoul 04763, Republic of Korea. <sup>2</sup>Department of Materials Science and Engineering, Nano Science Technology Institute, Yonsei University, Seoul 03722, Republic of Korea. <sup>3</sup>Department of Mechanical Engineering (Integrated Engineering Program), Kyung Hee University, Gyeonggi-do 17104, Republic of Korea. <sup>4</sup>School of Materials Science and Engineering, Chonnam National University, Gwangju 61186, Republic of Korea

## Author contributions

W.B.I. designed the concept and experiments. H.J.K. and S.J. predominantly performed the synthesis and device experiments, respectively. W.B.I., H.J.K., S.Y. J., and J.-U.P. interpreted the results and wrote the manuscript. H.C. and D.C. carried out a cytotoxicity test and numerical simulation analysis and interpreted the results. J.Y.H. helped in analyzing the phosphor properties. H.B. C. aided in the synthesis of phosphor and characterization. Y.-G.P. helped perform device fabrication and characterization.

## Conflict of interest

The authors declare no competing interests.

## Publisher's note

Springer Nature remains neutral with regard to jurisdictional claims in published maps and institutional affiliations.

**Supplementary information** The online version contains supplementary material available at <https://doi.org/10.1038/s41427-022-00374-8>.

Received: 11 November 2021 Revised: 27 January 2022 Accepted: 25 February 2022

Published online: 25 March 2022

## References

- Banerji, S., Mehta, S. B. & Millar, B. J. Cracked tooth syndrome. Part 1: aetiology and diagnosis. *Br. Dent. J.* **208**, 459–463 (2010).
- Banerji, S., Mehta, S. B. & Millar, B. J. Cracked tooth syndrome. Part 2: restorative options for the management of cracked tooth syndrome. *Br. Dent. J.* **208**, 503–514 (2010).
- Ellis, S. G. S. Incomplete tooth fracture — proposal for a new definition. *Br. Dent. J.* **190**, 424–428 (2001).
- Zink, K. D. & Lieberman, D. E. Impact of meat and Lower Palaeolithic food processing techniques on chewing in humans. *Nature* **531**, 500–503 (2016).
- Batalha-Silva, S., Gondo, R., Stolf, S. C. & Baratieri, L. N. Cracked tooth syndrome in an unrestored maxillary premolar: a case report. *Oper. Dent.* **39**, 460–468 (2014).
- Wright, H. M. Jr et al. Identification of resected root-end dentinal cracks: a comparative study of transillumination and dyes. *J. Endod.* **30**, 712–715 (2004).
- Liewehr, F. R. An inexpensive device for transillumination. *J. Endod.* **27**, 130–131 (2001).
- Imbeni, V., Kruzic, J. J., Marshall, G. W., Marshall, S. J. & Ritchie, R. O. The dentin-enamel junction and the fracture of human teeth. *Nat. Mater.* **4**, 229–232 (2005).
- Liu, H. H. & Sidhu, S. K. Cracked teeth—treatment rationale and case management: case reports. *Quintessence Int.* **26**, 485–492 (1995).
- Mathew, S. et al. Diagnosis of cracked tooth syndrome. *J. Pharm. Bioallied Sci.* **4**, 242–244 (2012).
- Liang, X. et al. A comparative evaluation of cone beam computed tomography (CBCT) and multi-slice CT (MSCT) Part I. On subjective image quality. *Eur. J. Radio.* **75**, 265–269 (2010).
- Sasai, H., Iwai, H., Fujita, D., Seto, E. & Izumi, Y. The use of micro-computed tomography in the diagnosis of dental and oral disease in rabbits. *BMC Vet. Res.* **10**, 209 (2014).

13. Imai, K., Shimada, Y., Sadr, A., Sumi, Y. & Tagami, J. Noninvasive cross-sectional visualization of enamel cracks by optical coherence tomography in vitro. *J. Endod.* **38**, 1269–1274 (2012).
14. Kim, J.-M., Kang, S.-R. & Yi, W.-J. Automatic detection of tooth cracks in optical coherence tomography images. *J. Periodontal Implant Sci.* **47**, 41–50 (2017).
15. Jeong, S. M. et al. Bright, wind-driven white mechanoluminescence from zinc sulfide microparticles embedded in a polydimethylsiloxane elastomer. *Energy Environ. Sci.* **7**, 3338–3346 (2014).
16. Jeong, S. M., Song, S., Lee, S. K. & Ha, N. Y. Color manipulation of mechanoluminescence from stress-activated composite films. *Adv. Mater.* **25**, 6194–6200 (2013).
17. Feng, A. & Smet, A. P. F. A review of mechanoluminescence in inorganic solids: compounds, mechanisms, models and applications. *Materials (Basel)* **11**, 484 (2018).
18. Toby, B. H. EXPGUI, a graphical user interface for GSAS. *J. Appl. Crystallogr.* **34**, 210–213 (2001).
19. Momma, K. & Izumi, F. VESTA: a three-dimensional visualization system for electronic and structural analysis. *J. Appl. Crystallogr.* **41**, 653–658 (2008).
20. Zhang, J.-C., Long, Y.-Z., Yan, X., Wang, X. & Wang, F. Creating recoverable mechanoluminescence in piezoelectric calcium niobates through Pr<sup>3+</sup> doping. *Chem. Mater.* **28**, 4052–4057 (2016).
21. Zhang, H., Wei, Y., Huang, X. & Huang, W. Recent development of elastic-mechanoluminescent phosphors. *J. Lumin.* **207**, 137–148 (2019).
22. Zhang, H. W., Yamada, H., Terasaki, N. & Xu, C. N. Green mechanoluminescence of Ca<sub>2</sub>MgSi<sub>2</sub>O<sub>7</sub>: Eu and Ca<sub>2</sub>MgSi<sub>2</sub>O<sub>7</sub>: Eu, Dy. *J. Electrochem. Soc.* **155**, J55–J57 (2008).
23. Akiyama, M., Xu, C.-N. & Nonaka, K. Intense visible light emission from stress-activated ZrO<sub>2</sub>:Ti. *Appl. Phys. Lett.* **81**, 457–459 (2002).
24. Piconi, C. & Maccauro, G. Zirconia as a ceramic biomaterial. *Biomaterials* **20**, 1–25 (1999).
25. Hisbergues, M., Vendeville, S. & Vendeville, P. Zirconia: established facts and perspectives for a biomaterial in dental implantology. *J. Biomed. Mater. Res B Appl Biomater.* **88**, 519–529 (2009).
26. McCullough, J. D. & Trueblood, K. N. The crystal structure of baddleyite (monoclinic ZrO<sub>2</sub>). *Acta Crystallogr.* **12**, 507–511 (1959).
27. Smith, D. K. & Newkirk, W. The crystal structure of baddeleyite (monoclinic ZrO<sub>2</sub>) and its relation to the polymorphism of ZrO<sub>2</sub>\*. *Acta Crystallogr.* **18**, 983–991 (1965).
28. Pan, X., Yang, M. Q., Fu, X., Zhang, N. & Xu, Y. J. Defective TiO<sub>2</sub> with oxygen vacancies: synthesis, properties, and photocatalytic applications. *Nanoscale* **5**, 3601–3614 (2013).
29. Li, W., Liang, R., Hu, A., Huang, Z. & Zhou, Y. N. Generation of oxygen vacancies in visible light activated one-dimensional iodine TiO<sub>2</sub> photocatalysts. *RSC Adv.* **4**, 36959–36966 (2014).
30. Bilovol, V., Ferrari, S. & D. Derewnicka, F. D. Saccone, XANES and XPS study of electronic structure of Ti-enriched Nd–Fe–B ribbons. *Mater. Chem. Phys.* **146**, 269–276 (2014).
31. Chandra, B. P. Persistent mechanoluminescence induced by elastic deformation of ZrO<sub>2</sub>:Ti phosphors. *J. Lumin.* **130**, 2218–2222 (2010).
32. Cong, Y., Li, B., Lei, B. & Li, W. Long lasting phosphorescent properties of Ti doped ZrO<sub>2</sub>. *J. Lumin.* **126**, 822–826 (2007).
33. Kim, Y. H. et al. A zero-thermal-quenching phosphor. *Nat. Mater.* **16**, 543–550 (2017).
34. Huang, Y. P. & Lin, J. W. The trap bag concept of afterglow luminescence. *Sci. Rep.* **7**, 8475 (2017).
35. Gallino, F., Di Valentin, C. & Pacchioni, G. Band gap engineering of bulk ZrO<sub>2</sub> by Ti doping. *Phys. Chem. Chem. Phys.* **13**, 17667–17675 (2011).
36. Foster, A. S., Sulimov, V. B., Lopez Gejo, F., Shluger, A. L. & Nieminen, R. M. Structure and electrical levels of point defects in monoclinic zirconia. *Phys. Rev. B* **64**, 224108 (2001).
37. Xu, C.-N., Watanabe, T., Akiyama, M. & Zheng, X.-G. Direct view of stress distribution in solid by mechanoluminescence. *Appl. Phys. Lett.* **74**, 2414–2416 (1999).
38. Tiwari, N., Kuraria, R. K. & Kuraria, S. R. Mechanoluminescence induced by impulsive deformation in zirconium: Ti phosphor. *Radiat. Eff. Defects Solids* **170**, 679–689 (2015).
39. Kim, D. H. et al. Epidermal electronics. *Science* **333**, 838–843 (2011).
40. Zhang, Y. et al. Experimental and theoretical studies of serpentine microstructures bonded to prestrained elastomers for stretchable electronics. *Adv. Funct. Mater.* **24**, 2028–2037 (2014).
41. Someya, T., Dodabalapur, A., Gelperin, A., Katz, H. E. & Bao, Z. Integration and response of organic electronics with aqueous microfluidics. *Langmuir* **18**, 5299–5302 (2002).
42. Hurtado, A. et al. Transfer printing of semiconductor nanowire lasers. *IET Optoelectron.* **12**, 30–35 (2018).
43. Wang, C. et al. User-interactive electronic skin for instantaneous pressure visualization. *Nat. Mater.* **12**, 899–904 (2013).
44. Shin, S. H. et al. Integrated arrays of air-dielectric graphene transistors as transparent active-matrix pressure sensors for wide pressure ranges. *Nat. Commun.* **8**, 14950 (2017).
45. Pavani, K. et al. Highly efficient upconversion of Er(3+) in Yb(3+) codoped non-cytotoxic strontium lanthanum aluminate phosphor for low temperature sensors. *Sci. Rep.* **7**, 17646 (2017).